SCIENTIFIC REPORTS

OPEN

# Monolayer $PdSe_2$: A promising two-dimensional thermoelectric material

Received: 27 November 2017
Accepted: 26 January 2018
Published online: 09 February 2018

Dan Qin[1,2], Peng Yan[1], Guangqian Ding[3], Xujin Ge[2], Hongyue Song[2] & Guoying Gao[2]

**Motivated by the recent experimental synthesis of two-dimensional semiconducting film $PdSe_2$, we investigate the electronic and thermal transport properties of $PdSe_2$ monolayer by using the density functional theory and semiclassical Boltzmann transport equation. The calculated results reveal anisotropic transport properties. Low lattice thermal conductivity about 3 $Wm^{-1} K^{-1}$ (300K) along the *x* direction is obtained, and the dimensionless thermoelectric figure of merit can reach 1.1 along the *x* direction for *p*-type doping at room temperature, indicating the promising thermoelectric performance of monolayer $PdSe_2$.**

Thermoelectric materials, which enable a direct conversion between heat and electricity via either Seebeck or Peltier effect, have attracted much attention as a sustainable energy resource in the last decade[1]. The conversion efficiency of a thermoelectric material is quantified by the dimensionless thermoelectric figure of merit ($ZT$), which is defined as $ZT = S^2\sigma T/(\kappa_e + \kappa_l)$, where $S$ is the Seebeck coefficient, $\sigma$ the electrical conductivity, $T$ the absolute temperature, $\kappa_e$ and $\kappa_l$ the electronic and lattice thermal conductivities, respectively. Obviously, higher power factor ($PF = S^2\sigma$) and lower thermal conductivity are beneficial for improving the thermoelectric performance. The all-scale electronic and atomistic structural engineering techniques have been used to enhance $ZT$ values to 2 within a temperature range of 700 ~ 900 K[2–5]. Another promising simple structures exhibit intrinsically low thermal conductances without requiring sophisticate structural engineering such as SnSe crystal and with $ZT$ value of 2.6 at 923 K[6], although this value falls quickly for lower temperatures.

Since the discovery of graphene in 2004[7,8], many 2D structures of inorganic layered materials, such as black phosphorus[9–11] and h-BN[12,13] etc., have been experimentally realized during the last decade. It has been proposed that low-dimensional materials could have better thermoelectric performance than their bulk due to the diverse scattering mechanism for phonons and intrinsic energy dependence of their electronic density of states[14–16]. And even in high dimensional materials, one can make use of the effective low dimensionality of the electron band to increase the thermoelectric performance[17–19]. Recently, the class of transition metal dichalcogenide (TMD) with one layer of transition metal sandwiched between two layers of chalcogen atoms have been a subject of extensive studies due to their fantastic electronic properties[20–22]. However, the $ZT$ values of 2H- $MoSe_2$, $MoS_2$ and $WSe_2$ monolayers are about 0.1 at 1200 K[23], 0.11 at 500 K[24] and 0.7 at high temperature[23], respectively. It was confirmed that such a low $ZT$ is mainly caused by a high lattice thermal conductivity $\kappa_l$. While those with $CdI_2$ type typically represented by $M$ = Ti, Zr, Hf, etc. have much lower lattice thermal conductivities. For example, the $\kappa_l$ values of monolayer $ZrSe_2$ and $HfSe_2$ are 1.2 and 1.8 $Wm^{-1} K^{-1}$ [25], respectively at 300 K, leading to optimum $ZT$ values of 0.87 and 0.95, respectively.

Most recently, another class of layered materials formed by noble metals, such as Pt and Pd, with S and Se atoms have been investigated both experimentally and theoretically[26–30]. Importantly, the monolayer $PdSe_2$ has very recently been exfoliated from bulk crystals by Akinola D. Oyedele *et al.*[28], which is a pentagonal 2D layered noble transition metal dichalcogenide with a puckered morphology that is air-stable. The experimental results by Oyedele *et al.* demonstrated that few-layer $PdSe_2$ displayed tunable ambipolar charge carrier conduction with a high electron apparent field-effect mobility of ~158 $cm^2 V^{-1} s^{-1}$. In addition, the puckered 2D $PdSe_2$ flakes exhibit a widely tunable band gap that varies from metallic (bulk) to ~1.3 eV (monolayer). Motivated by this, we expand our knowledge on the thermoelectric properties on the monolayer $PdSe_2$ in this work. And to the best of our knowledge, there is no utter investigation in the thermoelectric properties of the monolayer $PdSe_2$. In this paper,

[1]Binzhou Medical University, Yantai, Shandong, 264003, P. R. China. [2]School of Physics, Huazhong University of Science and Technology, Wuhan, Hubei, 430074, P. R. China. [3]Chongqing University of Posts and Telecommunications, Chongqing, 400053, P. R. China. Dan Qin and Peng Yan contributed equally to this work. Correspondence and requests for materials should be addressed to D.Q. (email: qindan_ok@163.com)

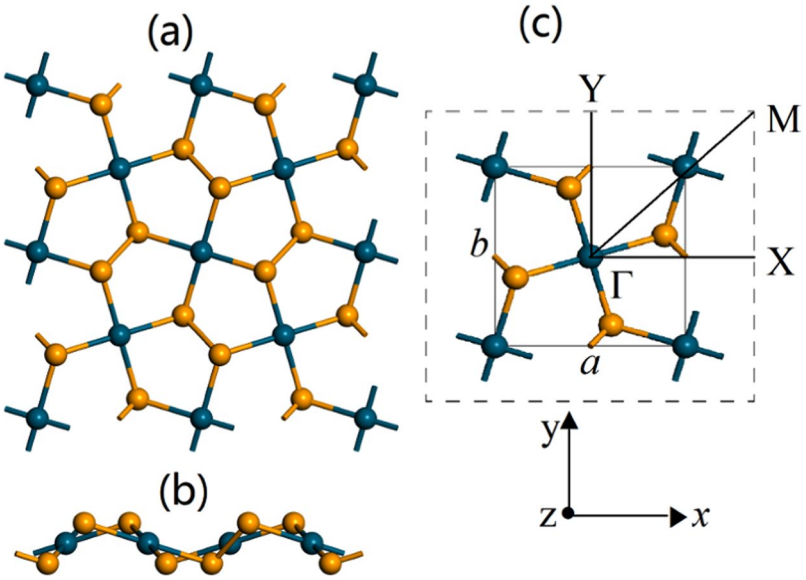


**Figure 1.** (**a**) and (**b**) are the top and side views of $PdSe_2$ monolayer, respectively. (**c**) The unit cell and corresponding Brillouin zone path with the high-symmetry points at Γ(0, 0, 0), X(0.5, 0, 0), M(0.5, 0.5, 0) and Y(0, 0.5, 0). The lattice parameters are denoted as *a* and *b*, which are along the *x* and the *y* directions, respectively. Cyan: Pd atom. Yellow:Se atom.

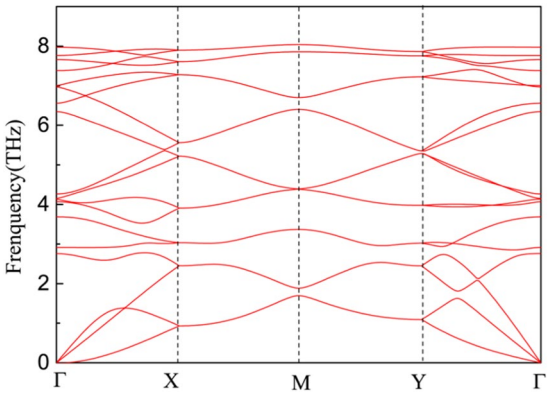


**Figure 2.** Calculated phonon dispersion spetrum of monolayer $PdSe_2$. Here the band structure is along the high-symmetry points at Γ(0, 0, 0), X(0.5, 0, 0), M(0.5, 0.5, 0), Y(0, 0.5, 0) and Γ(0, 0, 0).

we investigate $PdSe_2$ monolayer with the configuration of the above experiment, performing electronic structure, and phononic transport calculations based on density functional theory (DFT) and Boltzmann transport theory. The results show that monolayer $PdSe_2$ is an indirect semiconductor, with a band-gap value of 1.38 eV, which is in good agreement with ref.[28]. Based on the electronic and phononic properties, we study the thermoelectric properties of monolayer $PdSe_2$. We obtain the Seebeck coefficients for monolayer $PdSe_2$ and a maximum *p*-type figure of merit, 1.1, along the *x* direction at the optimal doping (300 K). We also find anisotropic characters in electrical conductivity and thermal conductivity which are derived from the asymmetric structure of the monolayer $PdSe_2$ in plane.

## Results and Discussions

**Geometric structure.** In our calculations, the monolayer structure is obtained from the experimental bulk structure $PdSe_2$ with $a = 5.75\,Å$, $b = 5.87\,Å$, and $c = 7.69\,Å$[31]. The monolayer $PdSe_2$ is cut through the (0 0 1) plane of the $PdSe_2$ crystal, and a vacuum slab about 21 Å is added in the direction perpendicular to the nano-sheet plane (*z* direction). As shown by the side view and projected top view of the $PdSe_2$ monolayer in Fig. 1(a) and (b), each Pd atom binds to four Se atoms in the same layer, two neighboring Se atoms can form a covalent Se-Se bond[32] and two Pd atoms and three S atoms can form a wrinkled pentagon, which is rather rare in known materials. In addition, we note that the space group has changed from *pbca* to $pca2_1$ evolving from bulk to monolayer, which has been found in experiments[27]. The unit cell of monolayer $PdSe_2$ is displayed in Fig. 1(c) and the optimized

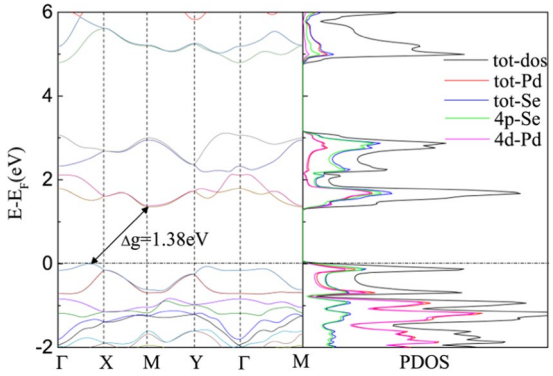


**Figure 3.** Calculated electronic band structure (left) and density of states (right) of monolayer $PdSe_2$ with indirect band gap of 1.38 eV. Here the band structure is along the high-symmetry points at Γ(0, 0, 0), X(0.5, 0, 0), M(0.5, 0.5, 0), Y(0, 0, 0.5) and Γ(0, 0, 0). The solid arrows indicate the lowest energy transitions between the valence band maximum (VBM) and conduction band minimum (CBM).

| directions | carriers | $m^*$ ($m_e$) | $m_d$ ($m_e$) | $C_{2D}$ (eV/$A^2$) | $E_l$(eV) | $\mu$ ($cm^2\ V^{-1}\ s^{-1}$) | $\tau$ ($10^{-14}$ $s$) |
|---|---|---|---|---|---|---|---|
| $x$ | e | 0.30 | 0.19 | 1.92 | −8.49 | 159.92 | 2.73 |
| | h | −0.25 | 0.20 | 1.92 | −2.61 | 1928.99 | 27.46 |
| $y$ | e | 0.12 | 0.19 | 1.17 | −9.11 | 211.59 | 1.44 |
| | h | −0.16 | 0.20 | 1.17 | −2.89 | 1498.03 | 13.64 |

**Table 1.** The computed effective mass ($m^*$), average effective mass ($m_d$), elastic modulus $C_{2D}$, DP constant $E_l$, carrier mobility ($\mu$), relaxation time ($\tau$) of electrons and holes along the $x$ and $y$ directions for the $PdSe_2$ monolayer at 300 K.

lattice parameters of monolayer $PdSe_2$ are $a = 5.7538\ Å$ and $b = 5.9257\ Å$, which are in good agreement with the previous reports[26,27].

In order to verify the stability of the monolayer $PdSe_2$, we perform phonon dispersion calculations[33]. As represented in Fig. 2, there are no soft modes in the calculated phonon dispersions, indicating the dynamical stability of this structure. This is also consistent with the previous reports[28,31].

**Electronic transport properties.** Experimental and theoretical studies have demonstrated that monolayer $PdSe_2$ exhibits high mobility and Seebeck coefficient[26,27], which are beneficial for the thermoelectric transport. Now we first turn to the investigation of electronic transport properties. Based on the above-determined configuration, we calculate the electronic band structure with the Brillouin zone path along $\Gamma - X - M - Y - \Gamma$ as shown in Fig. 1(c). Computed via the TB-mBJ-GGA potential with spin-orbit coupling (SOC) included, the $PdSe_2$ monolayer is semiconducting with an indirect band gap of 1.38 eV, which is in general agreement with the previous reports[26,34], as depicted in Fig. 3. The conduction band minimum (CBM) locates at the M (0.5, 0.5, 0) points, while the valence band maximum (VBM) locates in the interval between Γ and X (0.5, 0, 0) points. The projected density of states reveals that the $d$-states of the transition metal atoms and $p$-states of the selenium atoms contribute most to the states at both VBM and CBM.

The effective mass $m^*$ near the Fermi energy is an important parameter for the thermoelectric transport[35], which can be extracted from the high-precise energy band calculation via the equation

$$\frac{1}{m_\alpha^*} = \frac{1}{\hbar}\frac{\partial^2 E(k_a)}{\partial^2 k_\alpha} \tag{1}$$

where $\hbar$ is the reduced Plank's constant, $E(k_\alpha)$ is the band index $\alpha$ and wave vector k dependent energy. Thus, on the basis of the electronic band calculations, we can obtain the effective $m^*$ of electrons and holes in the $x$ and $y$ directions. As listed in Table 1, the effective mass along Γ-X and Γ-Y are 0.30(e), −0.25(h) and 0.12(e), −0.16(h), respectively. Obviously, in the $m_e$ unit of free electron mass, the effective masses along Γ-X are significantly larger than that along Γ-Y direction and even in the same direction there are slightly differences between holes and electrons, indicating the anisotropic electronic properties of monolayer $PdSe_2$. Besides the band gap and effective mass, carrier mobility is another important factor for semiconducting materials in electronic transport properties. Therefore, in order to obtain more information on the transport properties of monolayer $PdSe_2$, we investigate its carrier mobilities on the basis of Bardeen-Shockley deformation potential (DP) theory in 2D materials[36,37]. Note that the DP theory has been successfully performed to present the carrier mobility of many 2D structures[38–41]. Although the results may be less accurate, it can still reflect the basic and general thermoelectric performance of materials. According to the DP theory, the carrier mobility ($\mu$) of 2D structure can be expressed as

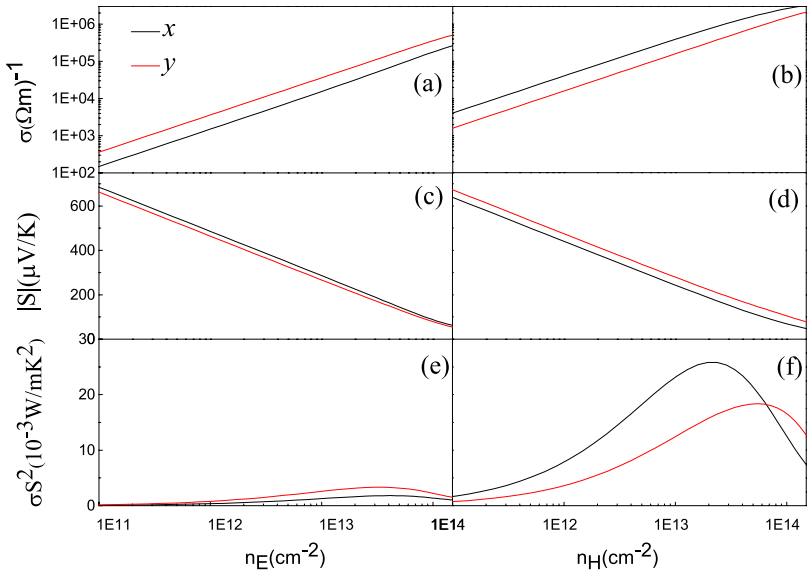


**Figure 4.** Calculated thermoelectric transport coefficients $\sigma$ (**a**,**b**), $S$ (**c**,**d**), and $S^2\sigma$ (**e**,**f**) vs carrier concentration for $n$-(left panels) and $p$-type (right panels) doped $PdSe_2$ along the $x$ (black lines) and the $y$ (red lines) directions at room temperature.

$$\mu = \frac{e\hbar^3 C_{2D}}{k_B T m^* m_d E_l^2} \tag{2}$$

where $k_B$ is the Boltzmann constant, $T$ is the temperature, $m_d$ is the average effective mass defined as $m_d = \sqrt{m_x^* m_y^*}$ ($m_x^*$ and $m_y^*$ are the effective mass along the $x$ and $y$ directions, respectively). $C_{2D}$ is the in-plane effective elastic modulus for 2D system defined as $C_{2D} = \frac{1}{S_0}\frac{\partial^2 E}{\partial(l/l_0)^2}|_{l=l_0}$, where $E$ and $l$ are the total energy and lattice constant after deformation, $l_0$ and $S_0$ are the lattice constant and cell area at equilibrium for 2D system. $E_l$ is the deformation potential constant determined by $E_l = \frac{\partial E_{edge}}{\partial(l/l_0)}|_{l=l_0}$, where $E_{edge}$ is the energy value of CBM (for electrons) and VBM (for holes). All the results are summarized in Table 1. The in-plane effective elastic modulus is 1.92 ($x$ direction) and 1.17 ($y$ direction) eV/Å$^2$ much lower than those of $MoS_2$ (7.99 eV/Å$^2$)[39] and $PdS_2$ (3.62 eV/Å$^2$ in the $x$ direction and 5.11 eV/Å$^2$ in the $y$ direction)[30], indicating that $PdSe_2$ is much softer than $MoS_2$ and $PdS_2$ monolayer. As have been investigated in previous works, such large flexible deformation may improve the electronic properties via the compression (tensile) strain[29,42–44]. By fitting the band edge-strain curves, we find that the deformation potentials ($E_l$) of holes are rather small, namely −2.61 ($x$ direction) and −2.89 ($y$ direction), compared with the values of electrons of −8.49 ($x$ direction) and −9.11 ($y$ direction) cm$^2$ V$^{-1}$ s$^{-1}$, respectively. Deformation potential constants describe the scattering caused by electron-acoustic phonon interactions. Thus, small of deformation potential constants may lead to large carrier mobilities. Then, based on the Equation 2, the acoustic phonon-limited carrier mobilities have been estimated. As shown in Table 1, the mobilities of electrons are 159.92 and 211.59 cm$^2$ V$^{-1}$ s$^{-1}$ in the $x$ and $y$ directions, respectively. Whereas the mobilities of holes are 1928.99 ($x$) and 1498.03 ($y$), which are much larger than those of electrons mainly due to the rather small $E_l$. However, the mobilities of both holes and electrons for the $PdSe_2$ monolayer are larger than those of the $MoS_2$[39] and $PdS_2$[30], indicating that the monolayer $PdSe_2$ would be a quite promising material for electronic and thermoelectric applications.

Now we are in a position to evaluate the electronic transport coefficients such as Seebeck coefficient $S$ and electrical conductivity $\sigma$, based on the CRTA Boltzmann theory. The left (right) panels of Fig. 4 show the transport coefficients along the $x$ and $y$ directions as a function of the electron (hole) concentration at $T = 300$ K. It is clear that the $\sigma$ in Fig. 4(a,b) increases with the increasing carrier concentration while the magnitude of $S$ in Fig. 4(c,d) decreases with doping. The electrical conductivity $\sigma$ of monolayer $PdSe_2$ exhibits remarkable anisotropic behaviors with $(\sigma_y/\sigma_x) \sim 2.3$ for $n$-type doping and $(\sigma_x/\sigma_y) \sim 2.4$ for $p$-type at $1.1 \times 10^{13}$ cm$^{-2}$ concentration. The calculated Seebeck coefficients along the $x$ and $y$ directions as a function of carrier concentration are shown in Fig. 4(c) and (d) for $n$- and $p$-type doping, respectively. We find a larger asymmetry of the Seebeck coefficient for $p$-type doping than for $n$-type doping, which is in good agreement with the recent report[26]. This anisotropy in the thermopower values in the two different directions might enable to design transverse thermoelctric device[45]. It is important to note that the Seebeck coefficients for both $n$- and $p$-type doped monolayer $PdSe_2$ are substantially high at room temperature, reaching a peak value of 660 $\mu V/K$ at an electron concentration around $1.25 \times 10^{11}$ cm$^{-2}$ and with an average value in the range of 300–340 $\mu V/K$. These values of $S$ for monolayer $PdSe_2$ compare favorably with those reported for some other 2D materials[30,39]. Figure 4(e) and (f) depict the power factor (PF) $S^2\sigma$ at room temperature along the $x$ and $y$ directions for $n$- and $p$-doped $PdSe_2$ monolayer, respectively. The results reflect significant anisotropy in the power factor with the $PF_x/PF_y \sim 1.9$ for $p$-type doping and

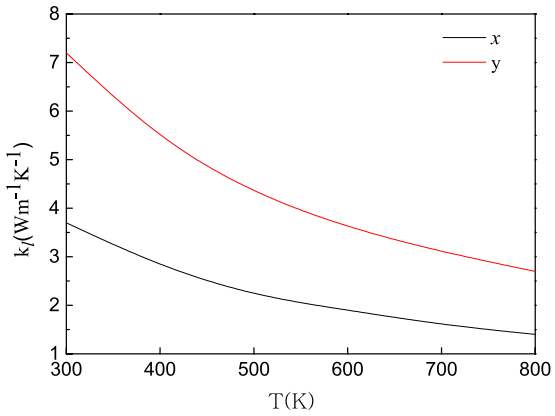


**Figure 5.** Calculated lattice thermal conductivity of monolayer $PdSe_2$ along the *x* (red solid line) and the *y* (black solid line) directions from 300 K to 800 K with the interval of 100 K.

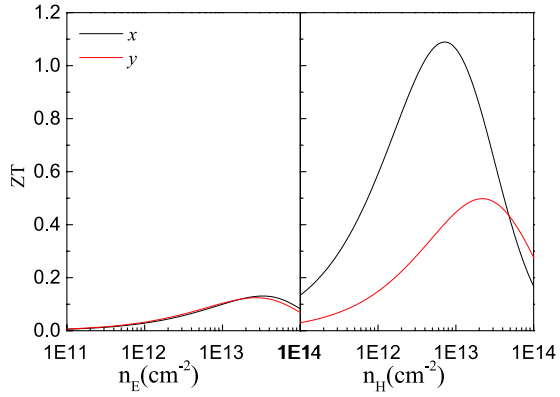


**Figure 6.** Calculated thermoelectric figure of merit (*ZT*) of monolayer $PdSe_2$ with *n*-type doping (left plane) and *p*-type doping (right plane) at 300 K along the *x* (black solid lines) and *y* (red solid lines) directions.

$(PF)_y/(PF)_x \sim 2$ for *n*-type doping at concentration around $1.1 \times 10^{13}\,cm^{-2}$. The anisotropy in power factor arises from the large anistotropy of the conductivity and Seebeck coefficient for *p* and *n* types, as described above.

**Phononic transport.** Figure 2 shows the phonon dispersion relations of monolayer $PdSe_2$ at its equilibrium volume along the high symmetric $\Gamma - Y - M - X - \Gamma$ directions. It is noteworthy that the phonon spectrums of monolayer $PdSe_2$ is very distinct from the $MoS_2$ type monolayer. The maximum frequency of the acoustic mode markedly drop to rather low value of 3.7 THz, while for monolayers of $MoSe_2$ and $WSe_2$ it is 5.4 THz and 4.8 THz, respectively, and even higher for monolayer $MoS_2$ with the value of 7.5 THz. Such low frequency suggests the low group velocity of acoustic modes in monolayer $PdSe_2$. As acoustic modes contribute mostly to the lattice thermal conductivity $\kappa_l$, lower $\kappa_l$ in this $PdSe_2$ monolayer is expected.

Now we turn to the computation of lattice thermal conductivity $\kappa_l$. As mentioned above, we estimate $\kappa_l$ by means of the phonon Boltzmann transport equation and DFT as implemented in VASP and ShengBTE code. As presented by the fitted lines in Fig. 5, $\kappa_l$ decreases following a $T^{-1}$ dependence with the increasing temperature, suggesting that Umklapp phonon scattering dominates three-phonon interactions[46]. From the calculations, the obtained lattice thermal conductivity of monolayer $PdSe_2$ is 3.7 (1.4) and 7.2 (2.7) $Wm^{-1}\,K^{-1}$ at 300 K (800 K) along the *x* and *y* directions, respectively, which are much lower than $MoS_2$[47] and $GX_2$ monolayers[48]. It is obvious that the lattice thermal conductivity exhibits large directional anisotropy which may be due to differences in group velocity, anharmonicity and scattering phase space along the different directions.

**Dimensionless figure of merit *ZT*.** The electronic thermal conductivity $\kappa_e$ of monolayer $PdSe_2$ is calculated via the Wiedemann-Franz law $\kappa_e = L\sigma T$. Within the relaxation time approximation, the Seebeck coefficient can be calculated independently of the relaxation time $\tau$, but evaluation of the electrical conductivity requires knowledge of $\tau$. Here we take into account only the intrinsic scattering mechanism, namely, the interaction of electrons with acoustic phonons. Then the relaxation time $\tau$ can be evaluated from the equation $\tau = \mu m^*/e$, here the carrier mobility $\mu$ and effective mass $m^*$ have been calculated in subsection of Electronic transport properties, as listed in Table 1.

Combining the electronic and thermal transport properties, we now evaluate the thermoelectric performance of the $PdSe_2$ monolayer. Figure 6 shows the figure of merit *ZT* value for both *n* and *p* doped $PdSe_2$ monolayer

along the $x$ and $y$ directions as a function of the carrier concentration at room temperature. We can see that the $ZT$ values of $n$-type doped monolayer $PdSe_2$ are rather small and almost isotropic with the maximum value of 0.13 with the corresponding concentration $3 \times 10^{13}\,cm^{-2}$. However, for $p$-type doped monolayer $PdSe_2$, $ZT$ values exhibit the strong anisotropic property, with the value along the $x$ direction being much larger than that along the $y$ direction. The largest $ZT$ value of 1.1 can be obtained in the $x$ direction at the carrier concentration of $6.5 \times 10^{12}\,cm^{-2}$ and 0.5 along the $y$ direction at the carrier concentration of $2 \times 10^{13}\,cm^{-2}$, respectively. Therefore, heavily doped $p$-type $PdSe_2$ may offer excellent thermoelectric performance for applications such as powergeneration. It is worthwhile to note that we have not considered the thermoelectric performance at higher temperature since the ZA mode of $PdSe_2$ monolayer is very soft near point Γ, hence, it may be difficult to remain stable at high temperature. Usually, the thermoelectric performance at room temperature is the most importantly information we need for it is better to discover thermoelectric materials working under room temperature.

## Conclusion

In summary, by means of first-principles calculation, the geometrical structure, mechanical, electronic and thermal transport properties of monolayer $PdSe_2$ are systematically investigated. In contrast to TMCs, monolayer $PdSe_2$ has strong anisotropic mechanical, electronic and thermal transport properties, leading to anisotropic thermoelectric properties. We find that $PdSe_2$ is a semiconductor with an indirect band gap of 1.38 eV and a hole mobility as high as $1929\,cm^2\,V^{-1}\,s^{-1}$. The in-plane effective elastic modulus are rather low, suggesting the flexible mechanical properties in this structure. Furthermore, monolayer $PdSe_2$ has a low lattice thermal conductivity about $3\,Wm^{-1}\,K^{-1}$ along the $x$ direction at room temperature. Combining its high Seebeck coefficient and markedly low thermal conductivity, monolayer $PdSe_2$ shows an optimum $ZT$ value of 1.1 (300K) at optimal doping. Therefore, our results indicate monolayer $PdSe_2$ is a material with promising thermoelectric performance.

## Computational Methods

The initial structure of monolayer $PdSe_2$ is optimized through DFT with the plane-wave based Vienna ab-initio simulation package (VASP)[49,50], using the projector augmented wave (PAW) method. For the exchange-correlation functional, we have used the Perdew-Burke-Ernzerhof version of the generalized gradient approximation (GGA)[51]. A plane-wave cutoff energy of 400 eV and an energy convergence criterion of $10^{-7}$ eV are adopted throughout calculations. The spin-orbit coupling (SOC) is not considered in the structure relaxation. For ionic relaxation calculations, a $11 \times 11 \times 1$ Monkhorst-Pack k-meshes[52] are used and the structure is considered to be stable when the Hellmann-Feynman forces are smaller than 0.001 eV/Å. For the slab model, a 21 Å thick vacuum layer was used to avoid the interactions between adjacent monolayers.

After determining the equilibrium structure, we have performed electronic structure calculations employing the all-electron full-potential WIEN2k code[53] using recently implemented Tran and Blaha's modified Becke-Johnson (TB-mBJ)[54] exchange potential plus generalised gradient approximation (GGA) with the SOC included. The TB-mBJGGA potential for electronic properties and band gap with higher accuracy and less computational effort as compared to hybrid functional and GW overcomes the shortcoming of underestimation of energy gap in both LDA and GGA approximations[55]. The number of plane waves in a Fourier expansion of potential in the interstitial region was restricted to $R_{MT} \times K_{max} = 8$. The muffin tin radii for Se and Pd are 2.1 and 2.2 a.u., respectively. We used $19 \times 19 \times 1$ k-point Monkhorst-Pack mesh for electronic band structure calculations.

Based on the self-consistent converged electronic structure calculations, we have employed the eigenenergies on a very dense nonshifted 8000 k-point mesh in the full Brillouin zone (BZ). Thermoelectrical transport properties were calculated by solving the Boltzmann transport equations within the rigid band (RBA) and constant relaxation-time approximations (CRTA) as implemented in the BoltzTraP software[56], which neglects the weak energy dependence of relaxation time but retains some temperature and doping dependence[57]. This CRTA approach has been tested earlier and found to work quite well in calculating the Seebeck coefficient in a variety of thermoelectric materials even for materials with highly anisotropic crystal axes[58–61]. A comprehensive description of the Boltzmann transport theory in the relaxation time approximation can be found elsewhere[23]. A brief summary of formalism used in this work is provided below[62]. The energy projected transport distribution (TD) tensor is defined as

$$\sigma_{\alpha\beta}(\varepsilon) = \frac{e^2}{N}\sum_{i,k}\tau_{i,k}v_\alpha(i,\,k)v_\beta(i,\,k)\delta(\varepsilon - \varepsilon_{i,k}) \tag{3}$$

where group velocity $v_\alpha(i,\,k) = \frac{1}{\hbar}\frac{\partial\varepsilon_{i,k}}{\partial k_\alpha}$, $N$ is the number of k-points sampled, $\tau_{i,k}$ is the band index $i$ and wave vector k dependent relaxation time, $\alpha$ and $\beta$ are the Cartesian indices, and $e$ is the electron charge. Then the electrical conductivity and Seebeck coefficient as a function of temperation $T$ and chemical potential $\mu$, can be written as

$$\sigma_{\alpha\beta}(T,\,\mu) = \frac{1}{\Omega}\int\sigma_{\alpha\beta}(\varepsilon)\left[-\frac{\partial f_0(T,\,\varepsilon,\,\mu)}{\partial\varepsilon}\right]d\varepsilon \tag{4}$$

$$S_{\alpha\beta}(T,\,\mu) = \frac{1}{e^2T\Omega}\sigma_{\alpha\beta}(T,\,\mu)\int\sigma_{\alpha\beta}(\varepsilon)(\varepsilon - \mu) \times \left[-\frac{\partial f_0(T,\,\varepsilon,\,\mu)}{\partial\varepsilon}\right]d\varepsilon \tag{5}$$

where $\Omega$ is the volume of unit cell and $f_0$ is the Fermi-Dirac distribution function. Thus, by using the CRTA, $\tau$ is exactly cancelled out in Equation 5. From the above calculations we can obtain the Seebeck coefficient

$S$ and the electrical conductivity over relaxation time ($\sigma/\tau$) as well. The electronic thermal conductivity $k_e$ is calculated using the Wiedemann-Franz law, $k_e = L\sigma T$, where $L$ is the Lorenz number. In our calculations we use $L = 2.4 \times 10^{-8} J^2 K^{-2} C^{-2}$ [63].

To confirm the dynamic stability of the $PdSe_2$ monolayer, we have calculated the phonon spectrum using a finite displacement method implemented the Phonopy code interfaced with the VASP code[50,64]. At the same time the second-order harmonic IFCs of monolayer $PdSe_2$ and third order anharmonic IFCs were calculated using a $4 \times 4 \times 1$ supercell and a $3 \times 3 \times 1$ supercell with $\Gamma$ point, respectively. Based on an adaptive smearing approach to the conservation of energy[65] and with an iterative solution method[66], we then solved the phonon Boltzmann transport equation using ShengBTE[67].

## References


1. Bell, L. E. Cooling, heating, generating power, and recovering waste heat with thermoelectric systems. *Science* **321**, 1457–1461 (2008).
2. Hsu, K. F. *et al*. Cubic agpbmsbte2+m: Bulk thermoelectric materials with high figure of merit. *Science* **303**, 818–821 (2004).
3. Biswas, K. *et al*. High-performance bulk thermoelectrics with all-scale hierarchical architectures. *Nature* **489**, 414–418 (2012).
4. Rhyee, J.-S. *et al*. Peierls distortion as a route to high thermoelectric performance in In4se3-[dgr] crystals. *Nature* **459**, 965–968 (2009).
5. Zhao, L., Dravid, V. & Kanatzidis, M. The panoscopic approach to high performance thermoelectrics. *Energ environ sci* **7**, 251–268 (2014).
6. Zhao, L.-D. *et al*. Ultralow thermal conductivity and high thermoelectric figure of merit in snse crystals. *Nature* **508**, 373–377 (2014).
7. Novoselov, K. S. *et al*. Electric field effect in atomically thin carbon films. *Science* **306**, 666–669 (2004).
8. Kane, C. L. Materials science: Erasing electron mass. *Nature* **438**, 168–170 (2005).
9. Li, L. *et al*. Black phosphorus field-effect transistors. *NatNano* **9**, 372–377 (2014).
10. Liu, H. *et al*. Phosphorene: An unexplored 2d semiconductor with a high hole mobility. *ACS Nano* **8**, 4033–4041 (2014).
11. Xia, F., Wang, H. & Jia, Y. Rediscovering black phosphorus as an anisotropic layered material for optoelectronics and electronics. *Nat. Commun.* **5**, 4458 (2014).
12. Zhi, C., Bando, Y., Tang, C., Kuwahara, H. & Golberg, D. Large-scale fabrication of boron nitride nanosheets and their utilization in polymeric composites with improved thermal and mechanical properties. *Adv. Mater.* **21**, 2889–2893 (2009).
13. Warner, J. H., Rümmeli, M. H., Bachmatiuk, A. & Büchner, B. Atomic resolution imaging and topography of boron nitride sheets produced by chemical exfoliation. *ACS Nano* **4**, 1299–1304 (2010).
14. He, J., Kanatzidis, M. G. & Dravid, V. P. High performance bulk thermoelectrics via a panoscopic approach. *Mater.Today* **16**, 166–176 (2013).
15. Zhang, J. *et al*. Phosphorene nanoribbon as a promising candidate for thermoelectric applications. *Sci. Rep.* **4**, 6452 (2014).
16. Park, K. H., Martin, P. N. & Ravaioli, U. Electronic and thermal transport study of sinusoidally corrugated nanowires aiming to improve thermoelectric efficiency. *Nat* **27**, 035401 (2016).
17. Wu, L. *et al*. Two-dimensional thermoelectrics with Rashba spin-split bands in bulk BiTeI. *Phys. Rev. B* **90**, 195210 (2014).
18. Mi, X.-Y. *et al*. Enhancing the Thermoelectric Figure of Merit by Low-Dimensional Electrical Transport in Phonon-Glass Crystals. *Nano Lett.* **15**, 5229–5234 (2015).
19. Bilc, D. I., Hautier, G., Waroquiers, D., Rignanese, G.-M. & Ghosez, P. Low-dimensional transport and large thermoelectric power factors in bulk semiconductors by band engineering of highly directional electronic states. *Phys. Rev. Lett.* **114**, 136601 (2015).
20. Butler, S. Z. *et al*. Progress, challenges, and opportunities in two-dimensional materials beyond graphene. *ACS Nano* **7**, 2898–2926 (2013).
21. Xu, M., Liang, T., Shi, M. & Chen, H. Graphene-like two-dimensional materials. *Chem. Rev.* **113**, 3766–3798 (2013).
22. Kuc, A. & Heine, T. The electronic structure calculations of two-dimensional transition-metal dichalcogenides in the presence of external electric and magnetic fields. *Chem. Soc. Rev.* **44**, 2603–2614 (2015).
23. Kumar, S. & Schwingenschlögl, U. Thermoelectric response of bulk and monolayer $MoSe_2$ and $Wse_2$. *Chem. Mater.* **27**, 1278–1284 (2015).
24. Jin, Z. *et al*. A revisit to high thermoelectric performance of single-layer $MoS_2$. *Sci. Rep*. **5** (2016).
25. Ding, G., Gao, G. Y., Huang, Z., Zhang, W. & Yao, K. Thermoelectric properties of monolayermse2(m = zr, hf): low lattice thermal conductivity and a promising figure of merit. *Nat* **27**, 375703 (2016).
26. Sun, J., Shi, H., Siegrist, T. & Singh, D. J. Electronic, transport, and optical properties of bulk and mono-layer $PdSe_2$. *Appl. Phys. Lett.* **107**, 153902 (2015).
27. Chow, W. L. *et al*. High mobility 2d palladium diselenide field-effect transistors with tunable ambipolar characteristics. *Adv. Mater.* **29**, 14090–14097 (2017).
28. Oyedele, A. *et al*. Pdse2: Pentagonal 2d layers with high air stability for electronics. *J.Am.Chem.Soc.* **0**, null (0).
29. Ahmad, S. Strain dependent tuning electronic properties of noble metal di chalcogenidespdx2(x = s,se)monolayer. *Mater. Chem. Phys.* **198**, 162–166 (2017).
30. Wang, Y., Li, Y. & Chen, Z. Not your familiar two dimensional transition metal disulfide: structural and electronic properties of the $PdS_2$ monolayer. *J. Mater. Chem. C* **3**, 9603–9608 (2015).
31. Soulard, C. *et al*. Experimental and Theoretical Investigation on the Relative Stability of the $PdS_2$- and Pyrite-Type Structures of $PdSe_2$. *Inorganic Chemistry* **43**, 1943–1949 (2004).
32. Grønvold, F. & Røst, E. The crystal structure of $PdSe_2$ and $PdS_2$. *Acta Crystallographica* **10**, 329–331 (1957).
33. Baroni, S., de Gironcoli, S., Dal Corso, A. & Giannozzi, P. Phonons and related crystal properties from density-functional perturbation theory. *Rev. Mod. Phys.* **73**, 515–562 (2001).
34. Lebègue, S., Björkman, T., Klintenberg, M., Nieminen, R. M. & Eriksson, O. Two-dimensional materials from data filtering and ab initio calculations. *Phys. Rev. X* **3**, 031002 (2013).
35. Pei, Y., LaLonde, A. D., Wang, H. & Snyder, G. J. Low effective mass leading to high thermoelectric performance. *Energy & Environmental Science* **5**, 7963 (2012).
36. Beleznay, F., Bogár, F. & Ladik, J. Charge carrier mobility in quasi-one-dimensional systems: Application to a guanine stack. *J. Chem. Phys.* **119**, 5690–5695 (2003).
37. Zhang, L.-C. *et al*. Tinselenidene: a two-dimensional auxetic material with ultralow lattice thermal conductivity and ultrahigh hole mobility. *Sci. Rep*. **6** (2016).
38. Long, M., Tang, L., Wang, D., Li, Y. & Shuai, Z. Electronic structure and carrier mobility in graphdiyne sheet and nanoribbons: Theoretical predictions. *ACS Nano* **5**, 2593–2600 (2011).
39. Cai, Y., Zhang, G. & Zhang, Y.-W. Polarity-reversed robust carrier mobility in monolayer mos2 nanoribbons. *J.Am.Chem.Soc.* **136**, 6269–6275 (2014).
40. Qiao, J., Kong, X., Hu, Z.-X., Yang, F. & Ji, W. High-mobility transport anisotropy and linear dichroism in few-layer black phosphorus. *Nat. Commun.* **5** (2014).

41. Wang, Y. *et al*. Monolayerptse2, a new semiconducting transition-metal-dichalcogenide, epitaxially grown by direct selenization of pt. *Nano Letters* **15**, 4013–4018 (2015).
42. Qin, D., Ge, X.-J., Ding, G.-Q., Gao, G.-Y. & Lü, J.-T. Strain-induced thermoelectric performance enhancement of monolayer $ZrSe_2$. *RSC Adv.* **7**, 47243–47250 (2017).
43. Guo, H., Lu, N., Wang, L., Wu, X. & Zeng, X. C. Tuning electronic and magnetic properties of early transition-metal dichalcogenides via tensile strain. *J.Phys.Chem. C* **118**, 7242–7249 (2014).
44. Guo, S.-D. Biaxial strain tuned thermoelectric properties in monolayer $PtSe_2$. *J. Mater. Chem. C.* **4**, 9366–9374 (2016).
45. Zhou, C., Birner, S., Tang, Y., Heinselman, K. & Grayson, M. Driving perpendicular heat flow: $(p \times n)$-type transverse thermoelectrics for microscale and cryogenic peltier cooling. *Phys. Rev. Lett.* **110**, 227701 (2013).
46. Ward, A., Broido, D. A., Stewart, D. A. & Deinzer, G. Ab initio. *Phys. Rev. B* **80**, 125203 (2009).
47. Yan, R. *et al*. Thermal Conductivity of Monolayer Molybdenum Disulfide Obtained from Temperature-Dependent Raman Spectroscopy. *ACS Nano* **8**, 986–993 (2014).
48. Ge, X.-J., Qin, D., Yao, K.-L. & Lü, J.-T. First-principles study of thermoelectric transport properties of monolayer gallium chalcogenides. *Journal of Physics D: Applied Physics* **50**, 405301 (2017).
49. Kresse, G. & Hafner, J. Ab initio. *Phys. Rev. B* **47**, 558–561 (1993).
50. Kresse, G. & Furthmüller, J. Efficient iterative schemes for ab initio total-energy calculations using a plane-wave basis set. *Phys. Rev. B* **54**, 11169 (1996).
51. Perdew, J. P., Burke, K. & Ernzerhof, M. Generalized gradient approximation made simple. *Phys. Rev. Lett.* **77**, 3865–3868 (1996).
52. Monkhorst, H. J. & Pack, J. D. Special points for brillouin-zone integrations. *Phys. Rev. B* **13**, 5188–5192 (1976).
53. Blaha, P., Schwarz, K., Madsen, G., Kvasnicka, D. &Luitz, J. wien2k. *WIEN2k An augmented plane wave + local orbitals program for calculating crystal properties* (2001).
54. Tran, F. & Blaha, P. Accurate band gaps of semiconductors and insulators with a semilocal exchange-correlation potential. *Phys. Rev. Lett.* **102**, 226401 (2009).
55. Kim, Y.-S., Marsman, M., Kresse, G., Tran, F. & Blaha, P. Towards efficient band structure and effective mass calculations for iii-v direct band-gap semiconductors. *Phys. Rev. B* **82**, 205212 (2010).
56. Madsen, G. K. & Singh, D. J. Boltztrap. a code for calculating band-structure dependent quantities. *Comput. Phys. Commun.* **175**, 67–71 (2006).
57. Parker, D. & Singh, D. J. Potential thermoelectric performance from optimization of hole-doped $bi_2se_3$. *Phys. Rev. X* **1**, 021005 (2011).
58. Xi, L. *et al*. Chemical bonding, conductive network, and thermoelectric performance of the ternary semiconductors $cu_2snX_3$ ($x =$ se, s) from first principles. *Phys. Rev. B* **86**, 155201 (2012).
59. Singh, D. J. Electronic and thermoelectric properties of $CuCoo_2$: Density functional calculations. *Phys. Rev. B* **76**, 085110 (2007).
60. Parker, D. & Singh, D. J. High-temperature thermoelectric performance of heavily doped pbse. *Phys. Rev. B* **82**, 035204 (2010).
61. Wang, Y. *et al*. Enhanced thermoelectric performance of pbte within the orthorhombic *pnma* phase. *Phys. Rev. B* **76**, 155127 (2007).
62. Scheidemantel, T. J., Ambrosch-Draxl, C., Thonhauser, T., Badding, J. V. & Sofo, J. O. Transport coefficients from first-principles calculations. *Phys. Rev. B* **68**, 125210 (2003).
63. Parlinski, K., Li, Z. Q. & Kawazoe, Y. First-principles determination of the soft mode in cubic $zero_2$. *Phys. Rev. Lett.* **78**, 4063–4066 (1997).
64. Togo, A., Oba, F. & Tanaka, I. First-principles calculations of the ferroelastic transition between rutile-type and cacl 2-type sio 2 at high pressures. *Phys. Rev. B* **78**, 134106 (2008).
65. Li, W. *et al*. Thermal conductivity of diamond nanowires from first principles. *Phys. Rev. B* **85**, 195436 (2012).
66. Li, W., Lindsay, L., Broido, D., Stewart, D. A. & Mingo, N. Thermal conductivity of bulk and nanowire mg 2 si x sn 1- x alloys from first principles. *Phys. Rev. B* **86**, 174307 (2012).
67. Li, W., Carrete, J., Katcho, N. A. & Mingo, N. Shengbte: A solver of the boltzmann transport equation for phonons. *Comput. Phys. Commun.* **185**, 1747–1758 (2014).


## Acknowledgements

The authors gratefully acknowledge the financial supports from the National Natural Science Foundation of China (Grant No. 51401031).

## Author Contributions

D.Q. and P.Y. conceived and designed the research. D.Q. carried out the calculations and analyzed the calculated results with the helps from P.Y., G.Q.D., X.J.G. and H.Y.S. discussed the related calculated results. All authors reviewed the manuscript.

## Additional Information

**Competing Interests:** The authors declare no competing interests.

**Publisher's note:** Springer Nature remains neutral with regard to jurisdictional claims in published maps and institutional affiliations.